Research Article Vol. 34, No. 2 / 26 Jan 2026 / Optics Express 2450

Optics EXPRESS

Directional Smith-Purcell radiation via coupled high-index gratings

THOMAS DELPLACE,[1,2] ILYES BOUANATI,[1] GILLES ROSOLEN,[1] AND BJORN MAES[1,3]

[1]*Micro- and Nanophotonic Materials Group, Research Institute for Materials Science and Engineering, University of Mons, Place du Parc 20, 7000 Mons, Belgium*
[2]*Thomas.Delplace@umons.ac.be*
[3]*Bjorn.Maes@umons.ac.be*

Abstract: The emission of light when an electron passes by a periodic photonic structure, called Smith–Purcell radiation (SPR), creates new types of adjustable light sources. Here, we investigate directional or asymmetric SPR from a high-index dielectric double-grating structure. By introducing a lateral shift between the two gratings, we break the symmetry and enable directional emission through interference between coupled Bloch modes, thus without the need for a mirror-type structure as in previous designs. Using full-wave simulations and eigenmode analysis, we identify the modes responsible for radiation and describe their coupling properties. A coupled mode theory (CMT) model is developed to capture the transition between symmetric and asymmetric regimes, offering fast and intuitive insight into the emission behavior. This work highlights a compact and efficient approach for controlling SPR directionality in dielectric photonic structures.

1. Introduction

Smith-Purcell radiation (SPR) is a well-known phenomenon in electrodynamics, arising from the interaction between an electron beam and a periodic surface. Since its discovery in 1953 [1], SPR has attracted increasing attention due to its potential applications in the development of compact and tunable terahertz radiation sources, as well as in high-resolution spectroscopy and imaging. The ability of SPR to generate coherent radiation over a broad spectral range makes it a particularly attractive tool for non-destructive diagnostic systems and wakefield accelerators [2–11].

In the past, the study of SPR has primarily focused on metallic gratings [12–20]. Recent research on SPR has explored various geometrical configurations and materials to enhance emission efficiency. In particular, the use of dielectric photonic crystals [21–23] offers improved control over dispersion and radiation directionality [24–26], thereby opening new avenues for the design of compact and high-performance light sources. Structures supporting Bound States in the Continuum (BICs) [11,27] have also enabled enhanced emission in photonic crystals. Furthermore, SPR has mainly been studied in symmetric metallic structures, but some works investigated asymmetric configurations using Bragg mirrors or more complex geometries [25,26,28]

In this work, we propose a design that achieves directionality via interference between two shifted dielectric gratings, without the need for Bragg-type extra mirrors. We propose a structure composed of two high-index gratings positioned face to face, with the electron beam in between. Each grating consists of high-index bars placed on a thin layer of small index, itself deposited on a high-refractive-index substrate (Fig. 1(a)). We demonstrate that by laterally shifting the two gratings, it is possible to achieve one-way radiation without the need for any additional structure [25,26,29]. Thus, by breaking the top-down symmetry, we are able to generate asymmetric

#579024 https://doi.org/10.1364/OE.579024
Journal © 2026 Received 15 Sep 2025; revised 20 Nov 2025; accepted 22 Dec 2025; published 20 Jan 2026

Optics EXPRESS

radiation purely through interference effects [30], enabling distinct upward and downward radiation while maintaining a relatively simple structure.

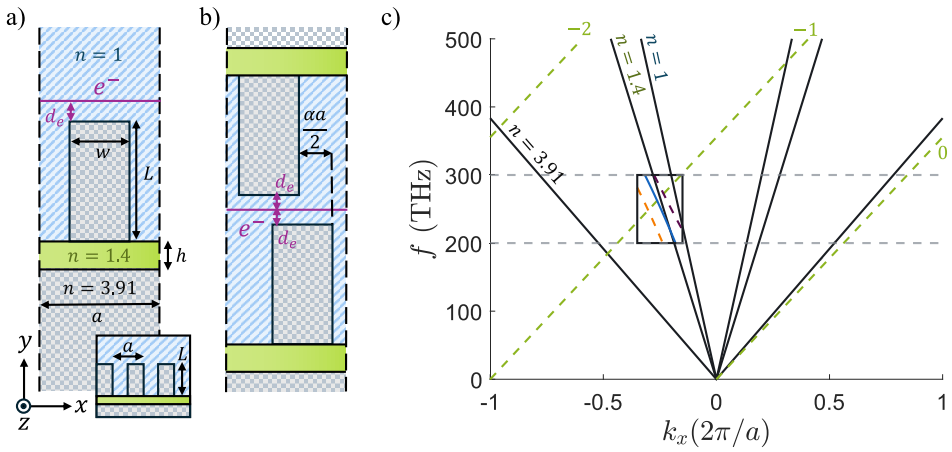

Fig. 1. (a) Unit cell of the single grating, periodic along x (periodic repetition in inset). (b) Unit cell of the double grating. The parameter α allows tuning the offset between the two gratings. (c) The black lines represent the light cones corresponding to refractive indices $n = 3.91$, $n = 1.4$, and $n = 1$, respectively. The green dashed lines indicate the different orders for an electron beam of 15 keV. The blue solid curve shows the dispersion for the single grating (solid line), and the orange and purple dashed lines for the double grating. The black rectangle shows the region of interest (zoom in Fig. 4(b)).

To better understand the physics at play, we introduce a model based on Coupled Mode Theory (CMT) [31–33]. This approach provides deeper insight into interference and coupling phenomena between the electromagnetic modes and opens new perspectives for optimizing SPR-based devices. We describe the emission via the analysis of Bloch modes guided within the structure, which is also the basis for the CMT model, allowing for fast and semi-analytical qualitative studies. For example, the thickness of the intermediate low-index layer is crucial to modulate the amount of light coupling from the gratings into the sub- and superstrate, and provides an important way to optimize for specific applications.

This work thus contributes to a better understanding of the SPR mechanisms in high-index designs, and provides key elements for the development of tunable sources based on dielectric photonic crystals.

2. Method

The simulations were performed with COMSOL Multiphysics. The electron-beam simulations used a wavelength-domain study, whereas the Bloch modes were computed with an eigenmode solver. In both cases, Floquet periodicity was employed, and perfectly matched layers (PMLs) were used to model the exterior radiation continuum. The lateral cell size is designed to provide 2.5 effective wavelengths on each side of the grating (or double grating). The PMLs have a thickness of one effective wavelength on each side. Because 2D simulations are less resource-intensive, we used mesh elements with a maximum size of 10 nm, which is far smaller than the usual recommendation of 5–6 mesh elements per effective wavelength. The electron beam was simulated using a ‘Surface Current Density’ node.

Optics EXPRESS

3. Geometry and dispersion

We investigate two structures: one consisting of a single grating (Fig. 1(a)), and the other of a double grating (Fig. 1(b)), both with a periodicity of $a = 200$ nm. The unit cell is composed of a high-index 'tooth' ($n = 3.91$) with a height $L = 200$ nm and a width $w = 100$ nm, corresponding to a fill factor of 50%. The grating is placed on top of a small index layer ($n = 1.4$) with variable thickness h. The entire structure rests on a high-index substrate ($n = 3.91$) and is surrounded by air. We choose a non-dispersive, large index value ($n = 3.91$, also used in [23] e.g.) for theoretical convenience. However, the features presented in this paper do not change qualitatively under small variations of the high-index value. The color code in Fig. 1(a) and (b) indicates the different materials used, grey for the $n = 3.91$ material, green for the $n = 1.4$ material and blue for air.

Since our focus is on SPR, an electron beam propagates at a distance d_e above the top of the grating (purple line in Fig. 1(a), b). The second structure under study consists of a double grating (Fig. 1(b)), each grating having the same dimensions as the one described in Fig. 1(a). We introduce a new parameter, α, which represents the lateral offset between the two gratings. $\alpha = 0$ corresponds to perfectly aligned gratings, while $\alpha = 1$ corresponds to a perfect 'anti-phase' configuration. The structure is invariant along z, so we simulate a two-dimensional geometry.

Figure 1(c) shows the dispersion of our system. The three black cones correspond to the light cones for the different materials, with refractive indices $n = 3.91$, $n = 1.4$, and $n = 1$, respectively. The green dashed lines represent the different orders for an electron beam with an energy of 15 keV, corresponding to $\beta = u_0/c = 0.273$, which is the electron velocity u_0 normalized to the speed of light in free space c. This choice ensures that only the -1 SPR order lies within the light cone of the substrate over the frequency range of interest (200 THz to 300 THz, gray dashed lines in Fig. 1(c)), while the 0th order (corresponding to Cherenkov radiation) remains outside the cone.

Since the structures shown in Fig. 1(a) and (b) are periodic, they support Bloch modes. To identify them, we use an eigenmode solver of the finite element-based commercial software COMSOL Multiphysics. The dispersion for a low-index material layer of $h = 100$ nm is indicated by colored lines inside the rectangle: blue solid line for the single grating and dotted (orange and purple) lines for the double grating. The two modes present in the double structure originate from the coupling between modes of the single grating structure. Indeed, the doubled structure is composed of two coupled gratings, so the (blue) single-grating mode splits into two (orange and purple) distinct modes. This mechanism will be described in more detail in Section 5.

4. Single-grating results

We investigate the single grating excited by a 15 keV electron beam positioned at a distance $d_e = 20$ nm. The electron beam is modeled as a sheet current, invariant along z, with a current density j_e, thus preserving the overall invariance of the structure in the z direction (details in [24]). All simulations presented in this paper are performed with TM polarization.

Figure 2(a) shows the downward emission spectrum obtained through COMSOL frequency-domain simulations (points) for various low-index layer thicknesses h. Several features can be observed in this spectrum. The first is a peak located between 250 THz and 270 THz depending on the low-index material thickness h, corresponding to a resonance excited by the -1 SPR order. Furthermore, at 288 THz there is a sudden drop in the emission, which corresponds to the onset of the air light cone and thus marks the beginning of upward radiation from the structure. Before this drop, the electron (order -1) line lies outside the light cone in air, and thus no upward radiation from the structure is produced. Figure 2(b) and (c) display the field profiles at the resonance peak for a low-index material thickness of $h = 100$ nm and $h = 200$ nm, respectively,

Optics EXPRESS

showing in both cases one-way, backward radiation to the bottom (note that the electron moves to the right in this figure).

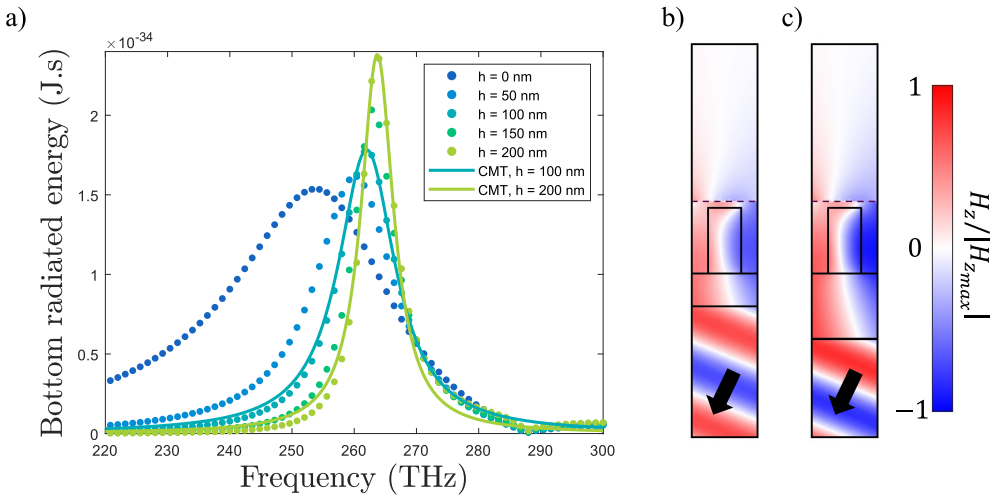

Fig. 2. (a) Downward emission spectrum of the structure for a single grating with different low-index material thicknesses h. Points represent COMSOL simulations using electron beam excitation. Solid lines indicate the CMT model. (b) and (c) Out-of-plane (z-direction) magnetic field profiles at the resonance peak with (b) $h = 100$ nm and (c) $h = 200$ nm.

By turning to eigenmode simulations, we obtain the Bloch modes of the structure, yielding the solid blue line in Fig. 1(c). The emission peak appears at the intersection between this mode and the electron line, indicating the excitation of the mode from the electron current. The intersection occurs at negative k_x values, resulting in radiation directed toward negative x, despite the electron propagating in the positive x direction (see Fig. 2(b) and (c)). The spectra in Fig. 2(a) also show that as h increases, the resonance peak becomes sharper and more intense, indicating a resonance with a higher quality Q-factor, due to the isolating effect of the low-index layer.

For the single-grating we can use the following single-mode CMT model [33]:

$$\frac{da}{dt} = (j\omega_0 - \gamma)a + s, \qquad a = a_0 e^{j\omega t}, \qquad s = s_0 e^{j\omega t}, \tag{1}$$

where a is the complex amplitude of the mode, ω_0 is the resonance angular frequency, γ represents the losses (due to radiation here), and s represents the amplitude of the electron source. By appropriately tuning these parameters, the CMT model fits well with the numerical spectra in Fig. 2(a). For $h = 100$ nm, we use $\omega_0 = 2\pi\ 262 \times 10^{12}$ rad/s and $\gamma = 0.35 \times 10^{14}$ rad/s. For $h = 200$ nm: $\omega_0 = 2\pi\ 263.6 \times 10^{12}$ rad/s and $\gamma = 0.2 \times 10^{14}$ rad/s.

5. Double-grating results

We now consider two gratings facing each other, see Fig. 1(b). Given the introduction of a new shift parameter α, we fix the low-index thickness $h = 100$ nm for clarity. The physics depends on this asymmetry parameter, so we divide the following description for the special cases ($\alpha = 0$ and 1) and the general case ($0 \leq \alpha \leq 1$).

5.1. Coupling between gratings: symmetrical cases

We focus on the two specific configurations with $\alpha = 0$ (gratings in phase) and $\alpha = 1$ (gratings in anti-phase). Both cases result in identical radiation intensity toward the top and bottom of the

Optics EXPRESS

structure. Figure 3(a) shows the downward spectra for $\alpha = 0$ (in purple) and $\alpha = 1$ (in orange). (Since the upward radiation is identical, it is not shown.) For both spectra, the distance between the gratings and the electron beam is $d_e = 20$ nm. Interestingly, there is only a single peak in the spectra, even though the two gratings are coupled.

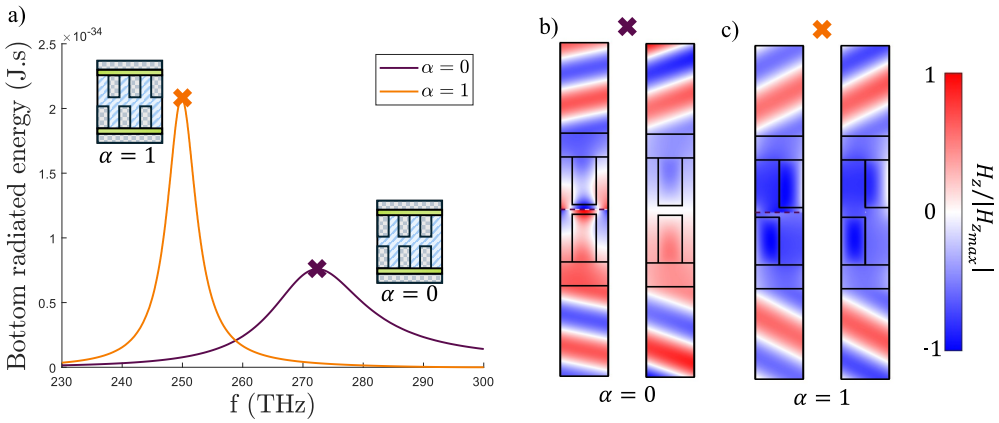

Fig. 3. (a) Emission spectra for $\alpha = 0$ (purple) and $\alpha = 1$ (orange) obtained from COMSOL. The two insets show the global structure for $\alpha = 0$ and $\alpha = 1$. (b) and (c) Magnetic field profiles excited by the electron (left) and the corresponding eigenmode (right) for (b) $\alpha = 0$ and (c) $\alpha = 1$. The purple and orange crosses correspond to the same resonance peaks as shown in a and Fig. 4.

Figure 3(b) and (c) show the field profiles corresponding to the two emission peaks marked with colored crosses. In both figures, the left profile corresponds to the magnetic field excited by the electron beam, obtained via a frequency-domain electron-beam simulation, while the right profile is obtained using COMSOL's eigenmode solver. A very strong similarity can be observed between the fields obtained by the two methods, reinforcing the hypothesis that the emission peaks correspond to the electron exciting a Bloch eigenmode. We also note that the field of the excited mode for $\alpha = 0$ (Fig. 3(b)) is top-bottom anti-symmetric, whereas the one excited for $\alpha = 1$ (Fig. 3(c)) is top-bottom symmetric. We will refer to them hereafter as the 'anti-symmetric mode' and the 'symmetric mode', respectively.

To link with the single grating structure, we compare the emission peak frequencies for varying distance d_e between the electrons and the grating(s) (and thus varying inter-grating distance $2d_e$), see Fig. 4(a). The purple curve corresponds to the peak position for $\alpha = 0$, the orange curve for $\alpha = 1$, and the blue curve for a single grating. The crosses correspond to the spectra illustrated in Fig. 3(a), i.e., for $d_e = 20$ nm. The single-grating emission peak (Fig. 4(a), in blue) is nearly constant, since varying d_e mainly alters the emission intensity, not the Bloch mode of the structure. In contrast, the double-grating peaks gradually deviate from the single grating as d_e decreases, indicating an increased coupling between the two gratings as the teeth approach each other.

To better understand this coupling, we analyze the Bloch mode dispersion of the double-grating structure. Figure 4(b) presents the single-grating (solid blue line) and double-grating dispersion (dashed purple and orange lines) for $d_e = 20$ nm (this is a zoom on the rectangle of Fig. 1(c)). Since the electron beam is absent during the Bloch mode calculation, d_e here refers to half the distance between the two gratings, i.e., the distance between the two gratings is 40 nm. The two dashed lines correspond to the Bloch modes in Fig. 3(b) and (c) (right), namely the anti-symmetric mode (purple cross) and the symmetric mode (orange cross), respectively. Note that both types of modes exist for all values of α (so not only for the special $\alpha = 0$ and 1 cases).

Optics EXPRESS

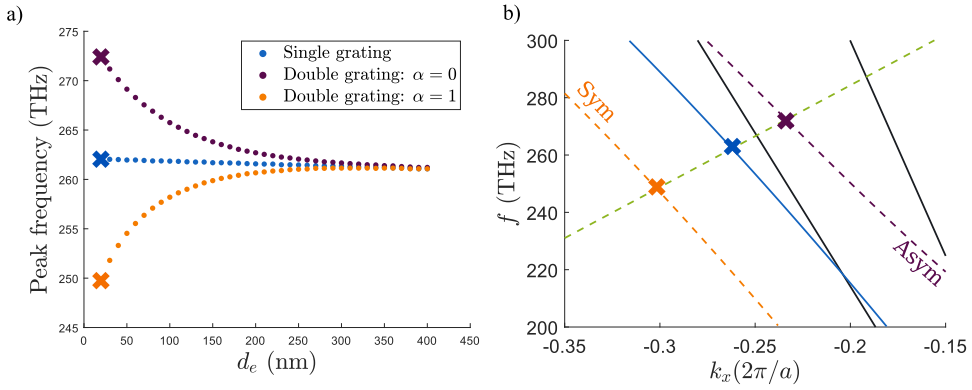

Fig. 4. (a) Resonance peak positions for a single grating (blue), a double grating with $\alpha = 0$ (purple), and with $\alpha = 1$ (orange). (b) Dispersion of the eigenmodes for the single grating (solid blue line) and the double grating (dashed purple and orange lines) at $d_e = 20$ nm. Green dashed line shows the electron order -1. Solid black lines indicate air (top) and $n = 1.4$ (bottom) light cones. In both (a) and (b), the colored crosses indicate the resonance peak positions for $d_e = 20$ nm.

Furthermore, the modes represented in Fig. 4(b) correspond to $\alpha = 0$, but the difference for other α values is very small.

The crosses in Fig. 4(b) indicate the intersection points between the -1th order SPR electron dispersion and the Bloch modes. Their positions match the observed resonance peak frequencies in the 'electron-excited' simulations for the different configurations (262 THz for the single grating, 272 THz for $\alpha = 0$, and 250 THz for $\alpha = 1$). Interestingly, for $\alpha = 0$, the dominant resonance corresponds to the anti-symmetric mode, whereas for $\alpha = 1$, it corresponds to the symmetric mode. This mode selection can be understood via the field profiles in Fig. 3(b) and (c). The purple mode exhibits an anti-symmetric field distribution with respect to the x-axis, while the orange mode is symmetric. Since the electron beam source magnetic field is up-down anti-symmetric, the in-phase double-grating situation ($\alpha = 0$) only excites the up-down anti-symmetric eigenmode, not the symmetric one. Inversely, the anti-phase double-grating case ($\alpha = 1$) only excites the up-down symmetric mode, and not the anti-symmetric one. We will see in the next section that for intermediate cases ($0<\alpha<1$) both modes are excited simultaneously.

5.2. *Asymmetric cases and coupled mode theory*

For values of α between 0 and 1, a vertical asymmetry is introduced, resulting in an imbalance between the upward and downward emission spectra. Figure 5 shows the emission spectra obtained via COMSOL (dots) and the fitted CMT model (solid lines, detailed later on) for various α values.

As α increases from 0 to 1, the system transitions from the excitation of the anti-symmetric mode at approximately 272 THz (purple cross in Fig. 3) to the symmetric mode at around 250 THz (orange cross in Fig. 3). Therefore, as α increases, the right-hand (larger frequency) peak decreases in favor of the left-hand (lower frequency) one, indicating a gradual transition from one supermode to the other. Furthermore, the right-hand peak looks wider than the left-hand one, similar to Fig. 3(a). This is consistent with the quality factors of the eigenmodes, which are about $Q = 14$ for the left mode and $Q = 5$ for the right mode.

Interestingly, the upward and downward emissions can become very different for α between 0 and 1, indicating a directionality in the two directions, superstrate versus substrate. This is especially the case for values of α close to 0 (e.g., Fig. 5(a)) or close to 1 (e.g., Fig. 5(d)).

Optics EXPRESS

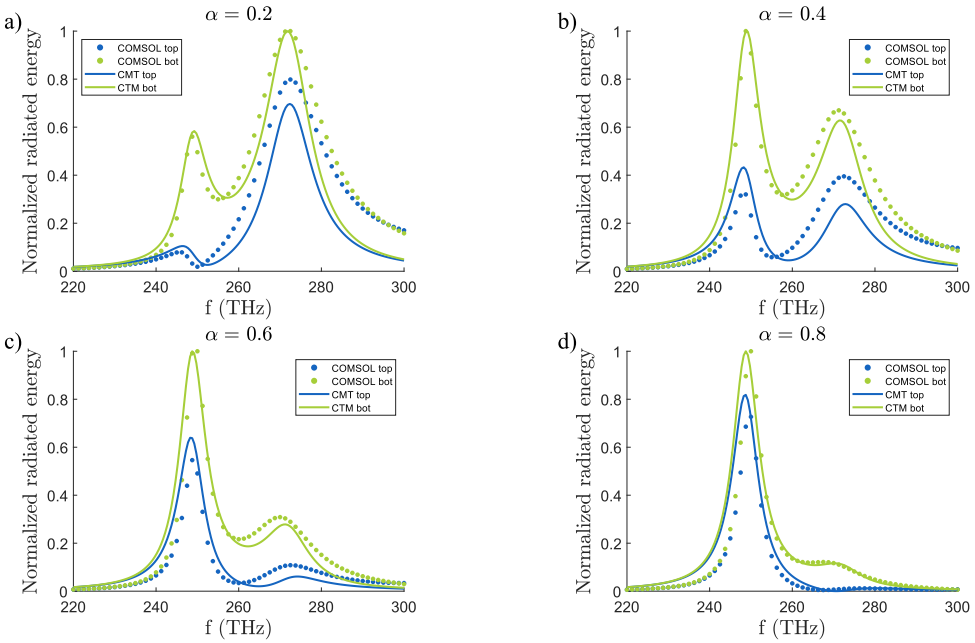

Fig. 5. Double-grating COMSOL simulations and CMT for (a) $\alpha = 0.2$, (b) $\alpha = 0.4$, (c) $\alpha = 0.6$, and (d) $\alpha = 0.8$. Blue indicates upward radiation, while red represents downward radiation. Dots correspond to COMSOL, solid lines to CMT.

Whereas the middle values of α (around 0.5) are more balanced (Fig. 3(b) and (d)). For example, for $\alpha = 0.2$, around 250 THz, there is very weak radiation to the top, and large radiation towards the bottom. These trends are explored in more detail in section 5.3.

Intuitively, each grating (mode) is excited by the electron beam, giving rise to a localized resonance in each. These two resonances can couple and interfere, leading to asymmetric emission. This hypothesis can be tested using a CMT model:

$$\frac{da_u}{dt} = (j\omega_0 - \gamma)a_u + j\kappa a_d + s_u, \quad a_u = a_{u0}e^{j\omega t}, \quad s_u = s_{u0}e^{j\omega t}, \tag{2}$$

$$\frac{da_d}{dt} = (j\omega_0 - \gamma)a_d + j\kappa a_u + s_d, \quad a_d = a_{d0}e^{j\omega t}, \quad s_d = s_{d0}e^{j(\omega t+\phi)}. \tag{3}$$

a_u and a_d denote the amplitudes of the two resonant modes connected with the separate 'up' and 'down' gratings, respectively, κ represents the coupling strength between the modes, s_u and s_d correspond to the source amplitudes driving each mode, with ϕ representing a potential phase shift due to the grating shift α.

By appropriately tuning these parameters, we obtain a satisfactory fit between the CMT model (dots in Fig. 5) and the COMSOL simulations (solid lines in Fig. 5), for various values of α. We use the following parameters: $s_{u0} = s_{d0} = 1$, $\omega_0 = 2\pi\ 262 \times 10^{12}$ rad/s, $\kappa = 0.475 \times 10^{14}$ rad/s and $\phi = \alpha\pi$. For γ it was necessary to account for the difference in losses between the two peaks, due to different Q factors mentioned earlier. Therefore, we replace the constant γ with a linear function, expressed as $\gamma(\omega) = -1.64 \times 10^{14}\text{rad/s} + 0.12\omega$. It has been shown that a frequency-dependent loss behavior is relevant in photonic crystals [34,35]. As the frequency increases, one approaches and enters the $n = 1.4$ light cone, thereby opening more channels for coupling out of the crystal and consequently increasing the losses. Within a narrow spectral window around each resonance, we therefore model this external-coupling trend by the mentioned

Optics EXPRESS

linear expression. This local law is not meant to be universal across the full band, but it compactly captures the observed increase of leakage with ω induced by substrate/superstrate coupling in the operating range of interest.

There is a slight difference in peak height observed between CMT and COMSOL. This discrepancy can be attributed to the presence of additional modes in the structure that are not accounted for in the model. This is noticeable on the right-hand side of the graphs in Fig. 5, where the emission does not drop to zero, indicating the presence of another weak resonance outside of the frequency range of interest.

Due to the good fit between the model and the (sometimes lengthy) simulations, we can use the CMT model to quickly extrapolate results for a broader range of parameters and generate parameter-space maps in seconds or minutes. Other parameters in the model can be tailored to different geometries. E.g., the parameter ϕ represents the phase difference between the two sources and is used to capture the influence of α on the system. Furthermore, by varying κ, we can model the increasing separation between the two gratings: the further apart they are, the weaker their coupling. Additionally, choosing $s_{u0} \neq s_{d0}$ allows for adjusting the relative amplitude of excitation, which can effectively model a shift of the electron beam away from the central position.

In our case the parameters κ and γ were determined by fitting the CMT model to the simulation results, and the value of ϕ followed intuitively from the geometrical interpolation. However, it should be possible to determine these parameters more rigorously from the modal field profiles, by using more advanced methods, e.g., as detailed in [36].

5.3. Model application

As indicated, the CMT model can quickly provide a large amount of information. As an example, we use it to qualitatively study the emission characteristics for different values of the important loss parameter γ. Figure 6(a) and (d) show the ratio between top and bottom emissions for $\gamma = \gamma_0$ and $\gamma = 2.5\gamma_0$, respectively, with γ_0 the linear loss function used for Fig. 5. The ratio a_u/a_d can be regarded as an asymmetry or directionality parameter: a value close to 1 (10^0, white color) indicates symmetry, while a large absolute value (or exponent, blue and red color) indicates strong asymmetry. In Fig. 6(a) and (d), intense red means a dominance of upward radiation, while intense blue means mainly downward radiation.

A significant qualitative difference is observed between Fig. 6(a) and (d). In Fig. 6(a), two distinct asymmetry peaks are visible around 250 THz and 275 THz, whereas in Fig. 6(d), a single asymmetry peak appears around 260 THz. This qualitative change as a function of loss suggests a regime transition with increasing γ_0, potentially enabling different application schemes. The regime in Fig. 6(a) corresponds with the discussion concerning the spectra as a function of α (Fig. 5): Values of α close to 0 and 1 provide the highest directionality.

Figure 6(b) and (c) show the upward and downward normalized emissions, respectively, for $\gamma = \gamma_0$, while Fig. 6(e) and (f) show the same for $\gamma = 2.5\gamma_0$. Figure 6(b) and (c) clearly illustrate the transition from the antisymmetric mode (higher frequency) at $\alpha = 0$ to the symmetric mode (lower frequency) at $\alpha = \pm 1$, as also depicted in Fig. 3. One can see that the left mode (symmetric) emits significantly more than the right mode (antisymmetric), consistent with Fig. 3.

As expected, lower losses result in sharper and more well-resolved peaks, while higher losses lead to broader, less distinct peaks. When these peaks broaden, they begin to overlap. In this overlapping regime, the coupling between the modes may be dominated by a simple additive contribution of the emissions from each individual mode.

Physically, modifying the value of γ can be realized by changing the thickness h of the low-index layer. Indeed, by increasing or decreasing h, we gain control over the quality of the resonances and thus over the height and width of the emission peaks (see Fig. 2(a)). Choosing a higher value of the losses γ, corresponding to a thinner low-index layer, can be useful due to

Optics EXPRESS

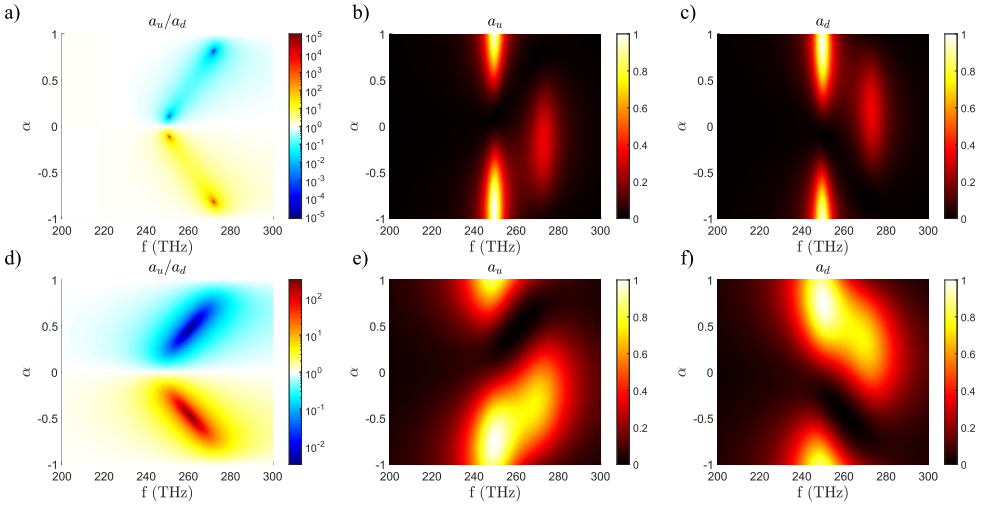

Fig. 6. (a)–(d) Ratio between the upward and downward emission amplitudes a_u/a_d. (b)–(e) Upward emission a_u. (c)–(f) Downward emission a_d. (a), (b), (c) Results for $\gamma = \gamma_0$ and (d), (e), (f) for $\gamma = 2.5\gamma_0$.

the qualitative difference between the two regimes: In one case, several asymmetry peaks in the frequency-α space are observed, while in the other, a single broad asymmetric region exists, enabling different behaviors depending on the chosen structure.

It is also possible to model the other geometrical parameters of the structure via the CMT model. Here we varied γ, which connects with the thickness of the low-index layer. For example, by adjusting κ, one can study the effect of the distance between the two gratings. Furthermore, by changing s_{u0} and s_{d0}, it is possible to simulate the impact of shifting the electron beam away from the central position. Finally, as mentioned earlier, ϕ is related to the lateral offset between the two gratings, namely α.

6. Conclusion

In this work, we investigate a dielectric double-grating structure composed of high-index teeth, demonstrating the generation of asymmetric Smith–Purcell radiation through the control of structural symmetry. By introducing a lateral offset between the two gratings, we show that the interference between coupled resonant modes enables directional emission without the need for additional elements or complex geometry.

We identify the key Bloch modes responsible for the observed emission features and describe their symmetry properties using both full-wave simulations and eigenmode analysis. By employing a Coupled Mode Theory framework, we develop a semi-analytical model capable of qualitatively reproducing the spectral asymmetries and explaining the transition from symmetric to asymmetric emission as the gratings are laterally shifted.

The agreement between the model and the numerical results validates the mode interference interpretation, and provides a compact, flexible tool for analyzing similar configurations. Furthermore, we use the model to explore the influence of radiative losses, revealing the potential for tailoring the radiation regime through simple parameter tuning.

By tuning the electron energy together with the geometric parameters of the structure, one can design the position and intensity of the resonance peaks. Varying the grating period modifies the Bloch-mode dispersion, enabling crossings with the electron light line at different frequencies.

Optics EXPRESS

Multiple peaks can also be generated by increasing the tooth height, providing broad design freedom and opening promising directions such as Moiré patterns or the study of chiral materials.

For fabrication, several routes are feasible. One approach is to etch the two photonic crystals on separate chips (along y) and then stack them, which allows the inter-grating spacing and the offset factor α to be adjusted as needed for the experiment. Another approach is to etch the whole structure at once in a single chip (in the z-direction) with relatively large depth. This method offers better dimensional accuracy but does not provide the flexibility to tune the structural parameters post-fabrication.

In the end, this study contributes to the fundamental understanding of SPR in photonic crystal-based systems and paves the way for the design of compact, directional, and tunable free-electron radiation sources leveraging dielectric nanostructures.

Disclosures. The authors declare no conflicts of interest.

Data availability. Data underlying the results presented in this paper are not publicly available at this time but may be obtained from the authors upon reasonable request.

References

1. S. J. Smith and E. M. Purcell, "Visible light from localized surface charges moving across a grating," Phys. Rev. **92**(4), 1069 (1953).
2. C. Roques-Carmes, S. E. Kooi, Y. Yang, *et al.*, "Free-electron-light interactions in nanophotonics," Appl. Phys. Rev. **10**(1), 011303 (2023).
3. I. Kaminer, S. Kooi, R. Shiloh, *et al.*, "Spectrally and spatially resolved smith-purcell radiation in plasmonic crystals with short-range disorder," Phys. Rev. X **7**(1), 011003 (2017).
4. A. Aryshev, A. Potylitsyn, G. Naumenko, *et al.*, "Monochromaticity of coherent smith-purcell radiation from finite size grating," Phys. Rev. Accel. Beams **20**(2), 024701 (2017).
5. P. Zhang, Y. Zhang, and M. Tang, "Enhanced thz smith-purcell radiation based on the grating grooves with holes array," Opt. Express **25**(10), 10901 (2017).
6. D. Y. Sergeeva, A. P. Potylitsyn, A. A. Tishchenko, *et al.*, "Smith-purcell radiation from periodic beams," Opt. Express **25**(21), 26310 (2017).
7. H. Zhang, I. Konoplev, and G. Doucas, "A coherent Smith-Purcell radiation source: design considerations for a high power, tunable source of terahertz radiation," *44th International Conference on Infrared, Millimeter, and Terahertz Waves* (IEEE, 2019).
8. N. V. Sapra, K. Y. Yang, D. Vercruysse, *et al.*, "On-chip integrated laser-driven particle accelerator," Science **367**(6473), 79–83 (2020).
9. A. Pupasov-Maksimov and D. Karlovets, "Smith-purcell radiation of a vortex electron," New J. Phys. **23**(4), 043011 (2021).
10. R. Rudzinsky, A. Debus, A. Irman, *et al.*, "Terahertz Smith-Purcell radiation from laser wakefield accelerated electron bunches," in *Advanced Accelerator Concepts Workshop* (IEEE, 2022), pp. 1–3.
11. D. Y. Sergeeva and A. A. Tishchenko, "Enhanced smith-purcell radiation based on quasibound states in the continuum in dimers aligned in a chain," Phys. Rev. B **108**(15), 155435 (2023).
12. E. L. Burdette and G. Hughes, "Smith-purcell radiation from small gratings," Phys. Rev. A **14**(5), 1766–1769 (1976).
13. J. H. Brownell and G. Doucas, "Role of the grating profile in smith-purcell radiation at high energies," Phys. Rev. Spec. Top.–Accel. Beams **8**(9), 091301 (2005).
14. A. S. Kesar, "Smith-purcell radiation from a charge moving above a finite-length grating," Phys. Rev. Spec. Top.–Accel. Beams **8**(7), 072801 (2005).
15. R. Remez, N. Shapira, C. Roques-Carmes, *et al.*, "Spectral and spatial shaping of smith-purcell radiation," Phys. Rev. A **96**(6), 061801 (2017).
16. A. Massuda, C. Roques-Carmes, Y. Yang, *et al.*, "Smith-purcell radiation from low-energy electrons," ACS Photonics **5**(9), 3513–3518 (2018).
17. P. Zhang, D. Zhao, X. Wang, *et al.*, "Smith-purcell radiation based on the transmission enhancement of a subwavelength hole array with inner tunnels," Opt. Express **29**(5), 7767 (2021).
18. Z. Yu, L. Zhang, W. Liu, *et al.*, "Coherent terahertz emission using metasurfaces to intercept a flat electron beam," Phys. Rev. Appl. **17**(1), 014038 (2022).
19. X. Zhang, T. Zhang, Z. Zhang, *et al.*, "Electron-beam-driven anomalous doppler effects in smith-purcell radiation," Photonics Res. **12**(1), 78 (2024).
20. Z. Sun, L. Cao, L. Wang, *et al.*, "Smith-purcell radiation in two dimensions," Phys. Rev. Lett. **134**(4), 043802 (2025).
21. S. Yamaguti, J. I. Inoue, O. Haeberlé, *et al.*, "Photonic crystals versus diffraction gratings in smith-purcell radiation," Phys. Rev. B **66**(19), 195202 (2002).
22. C. Roques-Carmes, S. E. Kooi, Y. Yang, *et al.*, "Towards integrated tunable all-silicon free-electron light sources," Nat. Commun. **10**(1), 3176 (2019).

Optics EXPRESS

23. D. Konakhovych, D. Sniezek, O. Warmusz, *et al.*, "Internal smith-purcell radiation and its interplay with cherenkov diffraction radiation in silicon – a combined time and frequency domain numerical study," arXiv (2021).
24. A. Szczepkowicz, L. Schächter, and R. J. England, "Frequency-domain calculation of smith-purcell radiation for metallic and dielectric gratings," Appl. Opt. **59**(35), 11146 (2020).
25. U. Haeusler, M. Seidling, P. Yousefi, *et al.*, "Boosting the efficiency of smith-purcell radiators using nanophotonic inverse design," ACS Photonics **9**(2), 664–671 (2022).
26. Z. Chen, L. Shao, L. Mao, *et al.*, "Rigorous coupled-wave analysis of unilateral smith-purcell radiation from asymmetric resonators," Appl. Opt. **63**(3), 708 (2024).
27. Y. Yang, A. Massuda, C. Roques-Carmes, *et al.*, "Maximal spontaneous photon emission and energy loss from free electrons," Nat. Phys. **14**(9), 894–899 (2018).
28. D. Li, Z. Yang, Y. Tsunawaki, *et al.*, "Improve growth rate of smith-purcell free-electron laser by bragg reflector," Appl. Phys. Lett. **98**(21), 211503 (2011).
29. Y. Sirenko, S. Sautbekov, M. Sautbekova, *et al.*, "Axial-symmetric diffraction radiation antenna with a very narrow funnel-shaped directional diagram," Appl. Sci. **11**(21), 10381 (2021).
30. T. Delplace and B. Maes, "Multimodal interference model for bound states in the continuum and unidirectional guided resonances," J. Opt. Soc. Am. B **42**(4), 840 (2025).
31. S. E. Miller, "Coupled wave theory and waveguide applications," Bell Syst. Tech. J. **33**(3), 661–719 (1954).
32. H. Haus, W. Huang, S. Kawakami, *et al.*, "Coupled-mode theory of optical waveguides," J. Lightwave Technol. **5**(1), 16–23 (1987).
33. H. Haus and W. Huang, "Coupled-mode theory," Proc. IEEE **79**(10), 1505–1518 (1991).
34. D. Gerace and L. C. Andreani, "Gap maps and intrinsic diffraction losses in one-dimensional photonic crystal slabs," Phys. Rev. E **69**(5), 056603 (2004).
35. N. Granchi, F. Intonti, M. Florescu, *et al.*, "Q-factor optimization of modes in ordered and disordered photonic systems using non-hermitian perturbation theory," ACS Photonics **10**(8), 2808–2815 (2023).
36. T. Christopoulos, O. Tsilipakos, and E. E. Kriezis, "Temporal coupled-mode theory in nonlinear resonant photonics: From basic principles to contemporary systems with 2d materials, dispersion, loss, and gain," J. Appl. Phys. **136**(1), 011101 (2024).